

Numerical study on the transient thermal performance of a lab-scale molten salt receiver

Cite as: J. Renewable Sustainable Energy **14**, 033701 (2022); <https://doi.org/10.1063/5.0085499>
Submitted: 17 January 2022 • Accepted: 20 April 2022 • Accepted Manuscript Online: 22 April 2022 •
Published Online: 09 May 2022

Zhonghua Huang, Yawei Li, Yifan Zhu, et al.



View Online



Export Citation



CrossMark

ARTICLES YOU MAY BE INTERESTED IN

[Output performance prediction of PV modules based on power-law model from manufacturer datasheet](#)

Journal of Renewable and Sustainable Energy **14**, 033501 (2022); <https://doi.org/10.1063/5.0088190>

[Power enhancement CFD based study of Darius wind turbine via roof corner placement](#)

Journal of Renewable and Sustainable Energy **14**, 033301 (2022); <https://doi.org/10.1063/5.0079971>

[Evaluation of energy storage systems for sustainable development of renewable energy systems—A comprehensive review](#)

Journal of Renewable and Sustainable Energy **14**, 032702 (2022); <https://doi.org/10.1063/5.0075623>



Numerical study on the transient thermal performance of a lab-scale molten salt receiver

Cite as: J. Renewable Sustainable Energy **14**, 033701 (2022); doi: 10.1063/5.0085499

Submitted: 17 January 2022 · Accepted: 20 April 2022 ·

Published Online: 9 May 2022



View Online



Export Citation



CrossMark

Zhonghua Huang,^{1,2} Yawei Li,¹ Yifan Zhu,¹ and Hao Zhou^{1,a)} 

AFFILIATIONS

¹State Key Laboratory of Clean Energy Utilization, Institute for Thermal Power Engineering, Zhejiang University, Hangzhou 310027, China

²Shanghai Electric Group Co. Ltd., Shanghai 201199, China

^{a)} Author to whom correspondence should be addressed: zhouhao@zju.edu.cn

ABSTRACT

The non-uniformity of temperature distribution and thermal stress distribution in the on-site high-temperature molten salt receiver is frequently reflected in the receiver's unstable operating circumstances. As a result, the focus of this research is on the transient thermal performance of the receiver in non-steady-state situations. An in-house software was used to estimate the transient temperature distribution of a lab-scale receiver using a three-dimensional transient model built for the receiver's thermal performance calculation. The transient thermal performance of a lab-scale receiver was studied under some variable operating conditions, such as the startup process, varying mass flow rate, varying radiation flux, and varying ambient wind speed, using a combination of numerical prediction and variable-condition experiment on a lab-scale receiver. When the working environment changed, the temperature distribution of the receiver took around 12 s to return to a stable condition. In addition, when the working environment changed, the transient temperature fluctuations of the receiver were given and evaluated in depth in this study.

Published under an exclusive license by AIP Publishing. <https://doi.org/10.1063/5.0085499>

I. INTRODUCTION

The high-temperature molten salt receiver is a critical component of the tower concentrated solar power (CSP) plant since it absorbs the heliostat field's converged sunlight by the molten salt flowing within the receiver.^{1,2} The surface of the receiver is frequently covered by very unequal radiant heat flux, resulting in an uneven distribution of the receiver's surface temperature, posing a challenge to the receiver's safe functioning. As a result, the thermal performance of the receiver must be investigated, and the temperature change of the molten salt must also be studied because it is directly connected to the CSP station's power output.^{3,4}

Much research had been conducted on the thermal performance of the solar center solar receiver.^{5–11} Zhang *et al.*¹² built a test system for an indoor cavity molten salt receiver and studied the effects of input power and mass flow rate of the molten salt on the receiver's temperature distribution, respectively. When the input power changes sharply, the maximum deviation between the experiment and the numerical value of the molten salt outlet temperature calculated was 66.32 °C, and the maximum relative error was 14.69%. A lab-scale receiver system was built by Zhou *et al.*,^{13,14} and its thermal performance was studied by using experimental measurement and mathematical models.

The results showed that the results obtained by simulation were consistent with the experimental results. Li *et al.*¹⁵ exploited the global steady-state models suitable for evaluating the thermal performance of cavity-type molten salt receivers and focused on the changes in the efficiency of the receiver under different factors, including the surface area of the receiver, the emissivity and reflectivity of the tube, the angle coefficient, and the number and size of tubes in the panel of the receiver.

The above literature mainly focuses on the steady-state or quasi-steady-state of the receiver, but they are also useful for unsteady research on the receiver. The receiver's preheating process is a typical transient process, which is the pre-processing of the normal operation of the CSP plants. Li *et al.*¹⁶ combined the methods of experiment and simulation to introduce the preheating process of the lab-scale receiver in detail. The preheating test of the lab-scale receiver under the constant heat flux density and the dynamic change heat flux density was carried out. In addition, they also conducted a preheating test of the receiver in a low-temperature environment and evaluated the effect of the ambient temperature on the receiver's preheating process. Fernández-Torrijos *et al.*^{17,18} used a molten salt loop heated by the induction heater to simulate the solar tower receiver's tubes and developed a transient numerical model to predict the temperature

distribution and the thermal stress distribution of the loop, and finally, a good coincidence between the experimental and calculated results was observed.

During the operation of the CSP station, the working environment of the receiver is prone to change, especially when the working conditions, such as salt charging, start and stop, and direct normal irradiance (DNI) change, and cloud cover occurs. When the working environment of the receiver changes, the transient thermal performance of the receiver needs to be simulated and calculated.^{19–22} Shen *et al.*²³ experimentally investigated a molten salt tubular receiver's transient heat transfer performance when its operating condition varied, and they found that the convective heat transfer of the molten salt varied and the dimensionless temperature evolution drastically changed when the flow velocity was changed. In addition, the Nusselt number of the molten salt flow is fitted with the Sieder–Tate equation at the beginning and end of the transient process. Xu *et al.*^{3,4} developed a set of 2D/three-dimensional (3D) transient models to calculate the receiver's transient thermal performance and found that the receiver could reach stabilizing after 35 s being filled with the salt. In addition, they also separately studied the transient thermal performance of the receiver under various unsteady conditions, such as startup phase, molten salt flow change, and thick cloud shelter, and all obtained satisfactory results. Augsburg and Favrat²⁴ modeled the effect of the cloud cover on the receiver's instantaneous incident flux distribution and presented a technique for determining the receiver's flux distribution. García *et al.*²⁵ investigated the dynamic performance of the central receiver under a novel targeting method for short-term cloud cover, which was combined with the DNI interference model. Because of the quickness of the DNI transient process, the results demonstrated that the basic closed-loop control may be applied to the steady-state operation, but it would result in unwanted overshoot and a greater heating rate. They discovered that instead of closed-loop control, a PI controller could successfully overcome the dynamic DNI changes produced by the cloud movement and assure the solar central receiver's safe functioning.

According to the above literature review, factors that frequently affect receivers in the process of an unsteady state include the start and

stop of the receiver, cloud cover, and wind speed changes. Therefore, methods for rapidly obtaining state performance changes of the receiver in the unsteady state are urgently needed. The transient temperature change of a lab-scale receiver in an unstable condition was investigated in this paper. This study proposes a novel calculation method for the receiver's unsteady thermal performance that completely incorporates the radiation heat transfer between the receiver's tubes as well as the boundary conditions of heat radiation and heat convection at the boundary. Furthermore, the mathematical findings and experimental data have been validated, which has important implications for the research of the receiver's unstable thermal performance. Finally, when the mass flow rate, direct normal irradiance (DNI), and wind speed varied, the transient temperature variations of the lab-scale receiver were described and discussed. The necessary data and calculation program were nonetheless of major importance to the safe operation of the on-site receiver, despite the fact that the study in this paper was done on a lab-scale receiver.

II. MATHEMATIC MODEL

A. Introduction of the lab-scale receiver

To study the transient thermal performance of the receiver, a laboratory-scale external molten salt receiver is built, as shown in Fig. 1(a). The receiver contains 18 Inconel 625 tubes, whose size is $\Phi 21 \times 1.2$ mm, and every three tubes form a panel, a total of six panels. The mass flow of 2.3 kg/s molten salt flows back and forth in these tubes six times and leaves the receiver. The section in the red rectangular frame in Fig. 1(a) is irradiated, and the other area is wrapped in thermal insulation cotton. The lab-scale receiver's light source is composed of 15 xenon lamps with adjustable power, and each xenon lamp's electric power could be adjusted in the range of 2–10 kW. Each xenon lamp can rotate in the horizontal and vertical planes by controlling its two axes. After adjustment, an uneven heat flux density distribution is obtained, and a hot spot is formed in the upper right corner, as shown in Fig. 1(b). This heat flux setting enables us to have a better understanding of the thermal performance of the receiver.

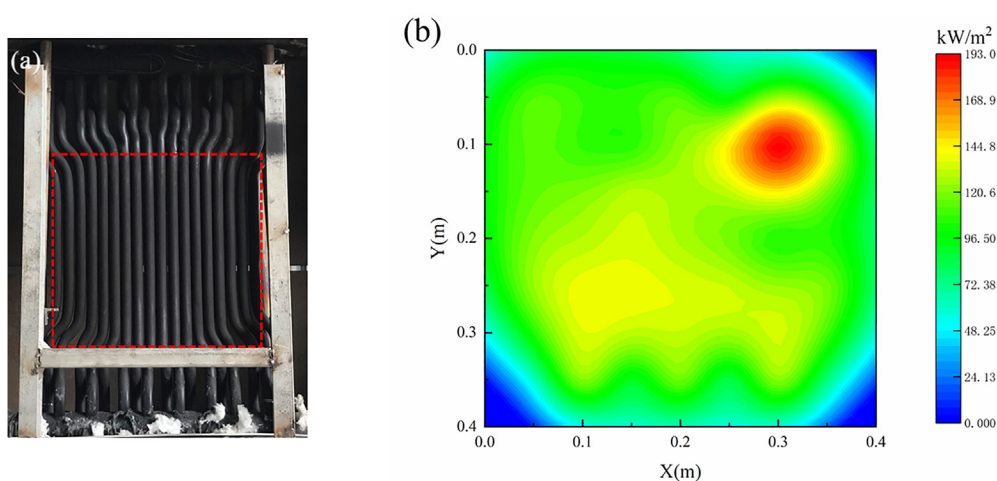


FIG. 1. The appearance of the lab-scale receiver and the flux map on the receiver.

B. Transient model

When the heat-absorbing tube is in use, the surface coating collects sunlight and distributes it by heat conduction to the pipe. Because the xenon lamps irradiate the front side of the receiver’s tube, exposing the surface to a high heat flux density, and the backside of the tube is next to the thermal insulation layer, the backside of the receiver’s tube can be considered adiabatic. Furthermore, molten salt scours the inside wall of the heat absorption tube at the same time as natural and forced convection to influence the surface of the outer tube wall. Furthermore, the high-temperature outer tube wall emits heat into the environment. The receiver’s transient temperature distribution must first be discretized before it can be calculated. The tube is split into $NR = 8$ pieces in the radial direction, which were numbered as $1, 2, \dots, m, \dots, NR$ from the inside to the outside, as shown in Fig. 2. Because the heat absorption tube’s temperature distribution is symmetrical along the input light direction, only half of the tube has to be addressed for modeling. As a result, the halfpipe was evenly divided into $NC = 60$ grids around the circumference, with the grids beginning at the back of the tube being numbered $1, 2, \dots, n, \dots, NC$.

Similarly, each tube was divided into $NZ = 61$ grids along the axial direction. Because the lab-scale receiver has six panels, the molten salt needs to pass $6 \times NZ$ grids from entering the receiver to leaving the receiver. In order to facilitate analysis, the axial grid of the tube was numbered as $1, 2, \dots, k, \dots, 6NZ$ along with the flow of molten salt. Therefore, the $[(j - 1) \times NZ + 1]$ th grid was the inlet of each tube, and the $(j \times NZ)$ th grid is the outlet of each tube, where j is the panel serial number with a value of 1–6. After division, any grid on the heat absorption tube can be represented by the coordinates (m,n,k) , and the temperature of any grid can be represented by $T(m,n,k)$, as shown in Fig. 2.

The grids that are not on the boundary will be impacted by the six grids around them on the tube, and there will be two heat fluxes in each direction, as illustrated in Fig. 2(b). The energy transported from the six networks will be received by the central grid. The aggregate of these energy transfers equals the rise or reduction of the volume’s thermal

energy in grid time $\Delta\tau$, according to the law of conservation of energy. The following equation may be derived from this connection:

$$\Phi_{r,+} + \Phi_{r,-} + \Phi_{\theta,+} + \Phi_{\theta,-} + \Phi_{z,+} + \Phi_{z,-} = \rho c_p \Delta V \frac{\Delta T}{\Delta \tau} \quad (1)$$

According to the knowledge of heat transfer, heat flow Φ could be regarded as the current, which could be calculated by the ratio of the temperature difference and thermal resistance, so the calculation of heat flow could be written as Eq. (2), where R is the thermal resistance,

$$\Phi = \frac{1}{R} \Delta T. \quad (2)$$

The circumferential and axial thermal resistance of the heat-absorbing tube is easier to calculate and could be expressed directly as δ/λ , where δ is the distance between the grids, m , and λ [W/(m K)] is the thermal conductivity. For the convenience of expression, we use K to represent the pre-coefficient of temperature difference, equal to $1/R$, which is also considered the heat conductance, so the circumferential pre-coefficient and the axial pre-coefficient are obtained as shown in Eqs. (3) and (4), respectively.

$$K_{\theta^-} = K_{\theta^+} = \frac{\lambda \Delta r \Delta Z}{r \Delta \theta}, \quad (3)$$

$$K_{z^-} = K_{z^+} = \frac{\lambda r \Delta r \Delta \theta}{\Delta Z}. \quad (4)$$

Since the surface area of the two adjacent elements in the radial direction is different, the radial thermal resistance calculation method is different from the calculation method of the circumferential and axial thermal resistance. The heat transfer between the radial adjacent elements could be simply thought of as one-dimensional radial heat conduction. According to the knowledge of heat transfer, the radial heat conduction and thermal resistance R (m^2 K/W) could be calculated by $R = \Delta S \cdot r_m \cdot \ln(r_{out}/r_{in})/\lambda$.²⁶ It could be seen that the radial heat conduction and thermal resistance are related to the radius of the grid. The radial pre-coefficients of the internal and external are shown

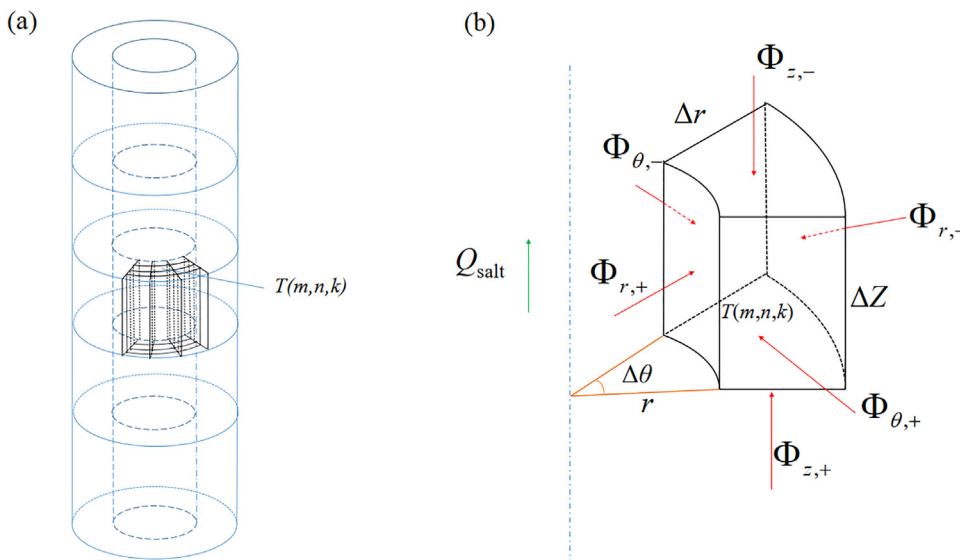


FIG. 2. Discretization of the tube and the inflow heat flow of the control volume.

in Eqs. (5) and (6), and similar methods were also used in the work of Fernández-Torrijos *et al.*,¹⁸

$$K_{r^-} = \frac{\lambda \Delta \theta \Delta Z}{\ln \left(\frac{r}{r - \Delta r} \right)}, \quad (5)$$

$$K_{r^+} = \frac{\lambda \Delta \theta \Delta Z}{\ln \left(\frac{r + \Delta r}{r} \right)}. \quad (6)$$

Therefore, the governing numerical difference equation of the tube wall temperature could be obtained by Eqs. (1)–(6), as shown in Eq. (7), where i represents the time series. To facilitate programming, Eq. (7) was converted to an explicit difference format, as shown in Eq. (8), where a is the thermal diffusivity of the tube,

$$\begin{aligned} & \frac{\lambda \Delta \theta \Delta Z}{\ln \left(\frac{r}{r - \Delta r} \right)} \left(T_{m-1,n,k}^i - T_{m,n,k}^i \right) \\ & + \frac{\lambda \Delta \theta \Delta Z}{\ln \left(\frac{r + \Delta r}{r} \right)} \left(T_{m+1,n,k}^i - T_{m,n,k}^i \right) \\ & + \frac{\lambda \Delta r \Delta Z}{r \Delta \theta} \left(T_{m,n+1,k}^i + T_{m,n-1,k}^i - 2T_{m,n,k}^i \right) \\ & + \frac{\lambda r \Delta r \Delta \theta}{\Delta Z} \left(T_{m,n,k+1}^i + T_{m,n,k-1}^i - 2T_{m,n,k}^i \right) \\ & = \frac{c_p \rho r \Delta r \Delta \theta \Delta Z}{\Delta \tau} \left(T_{m,n,k}^{i+1} - T_{m,n,k}^i \right), \quad (7) \end{aligned}$$

$$\begin{aligned} T_{m,n,k}^{i+1} &= \frac{a \Delta \tau}{r \Delta r \ln \left(\frac{r}{r - \Delta r} \right)} \left(T_{m-1,n,k}^i - T_{m,n,k}^i \right) \\ & + \frac{a \Delta \tau}{r \Delta r \ln \left(\frac{r + \Delta r}{r} \right)} \left(T_{m+1,n,k}^i - T_{m,n,k}^i \right) \\ & + \frac{a \Delta \tau}{(r \Delta \theta)^2} \left(T_{m,n+1,k}^i + T_{m,n-1,k}^i - 2T_{m,n,k}^i \right) \\ & + \frac{a \Delta \tau}{(\Delta Z)^2} \left(T_{m,n,k+1}^i + T_{m,n,k-1}^i - 2T_{m,n,k}^i \right) + T_{m,n,k}^i. \quad (8) \end{aligned}$$

However, Eq. (8) was only applicable to calculate the grid located not at the boundary, and it is not the same for the grid at the boundary of the tubes. Moreover, the grid's environment at the boundary is not the same, and it needs to be discussed one by one.

1. Import and export of heat absorption tube

The grid located at the entrance and exit of the tube had only one adjacent grid in the axial direction. In order to apply Eq. (8), it just needs to image a grid with the same temperature, that is, to set the incoming heat flow in the axial direction to 0.

2. The start and end of the circumferential direction

The tube was assumed to be symmetrical along the incident light direction to speed up the calculation, and only half of it was estimated throughout the calculation, leaving the circumferential direction open.

Imagine a single grid with the same temperature at the beginning and end of the circumferential direction, much as the grids at the tube's intake and exit.

3. The outer wall surface of the tube

When the pipes' outer wall receives the heat flow projected by the heliostat field, it also loses heat to the enclosures by thermal convection and radiation. Therefore, the grid located on the tubes' outer wall needs to be treated separately.

The lab-scale receiver's heat flux cast from the xenon lamps has been measured using the infrared camera and heat flow meter, as shown in Fig. 1(b). First, thermal analysis is performed on the outermost unit of the heat tubes, as shown in Fig. 3, where the environment is set as an imaginary surface. For i th unit, while absorbing the incoming radiation energy J , including the projected energy of the xenon lamp and the radiation energy of the surrounding units, it will also lose the energy q_{loss} , mainly including radiation loss and convective heat loss, as shown in Fig. 3(b). In the Z th short cylinder (Z is the number of the short cylinders divided by the tube along the axial direction), since the entire red line area in Fig. 3(b) can be regarded as a closed enclosure with input radiant heat flux from the xenon lamps, the net heat flux method, Eq. (9), was suitable to calculate the net inflow radiative heat flux $q_{NR,n,k}^i$ of each unit according to its temperature.^{9,13,27} The left side of Eq. (9) is the unknown quantity, and the right side is the known quantity. It is necessary to assume the temperature of each element of the tubes, and then the net inflow radiative heat flow of each element, namely, the heat absorbed by the molten salt, can be calculated by the following equation:

$$\begin{aligned} & m = 0, 1, \dots, N + 1, \\ & \left[\frac{\delta_{m,0}}{\varepsilon_0} - \left(\frac{1}{\varepsilon_0} - 1 \right) F_{m,0} \right] \frac{q_0}{\sigma} + \sum_{j=1}^N \left[\frac{\delta_{m,j}}{\varepsilon_j} - \left(\frac{1}{\varepsilon_j} - 1 \right) F_{m,j} \right] \frac{q_j}{\sigma} \\ & - [\delta_{m,N+1} - F_{m,N+1}] T_{N+1}^4 = [\delta_{m,0} - F_{m,0}] T_0^4 \quad (9) \\ & + \sum_{j=1}^N [\delta_{m,j} - F_{m,j}] T_j^4 - \left[\frac{\delta_{m,N+1}}{\varepsilon_{N+1}} - \left(\frac{1}{\varepsilon_{N+1}} - 1 \right) F_{m,N+1} \right] \frac{q_{N+1}}{\sigma} \\ & - F_{m,0} \frac{q_h''}{\sigma} (1 - \varepsilon). \end{aligned}$$

In Eq. (9), the subscript numbers $N + 1$ and 0 correspond to the insulating wall and the environmental surface, respectively, T represents the wall temperature of the unit, and F is the angle coefficient of the two units. δ stands for Kronecker delta, which is 1 when its subscripts are equal, and 0 when they are not equal. σ represents the Stefan-Boltzmann constant and takes the value of $5.67 \times 10^{-8} \text{ W m}^{-2} \text{ K}^{-4}$. The thermal insulation wall behind the heat sink is considered to be thermally insulated, $q_{N+1} = 0$. q_h'' is the projected radiant heat flow of the xenon lamp outside the red closed area in Fig. 3(b). T_0 is the ambient temperature, about 20°C .

The convection loss of the heat absorption tube could be divided into two parts, one is natural convection loss, and the other is forced convection loss. According to the knowledge of heat transfer, and the natural convection heat transfer coefficient $h_{n,air}$ of each grid could be calculated using Eq. (10), and the film temperature was selected as the reference temperature of the air,

$$Nu_{n,air} = 0.11 (Gr \cdot Pr)_m^{1/3}. \quad (10)$$

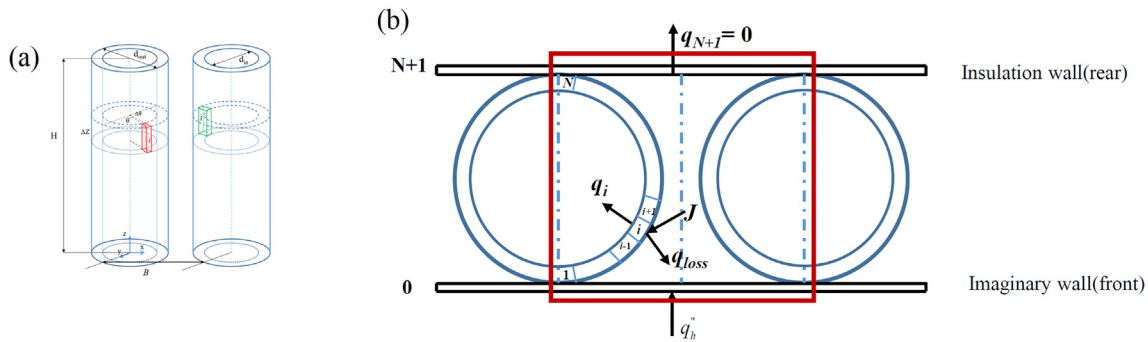


FIG. 3. Thermal analysis of elements on the outer wall of the tubes: (a) front view and (b) cross section of tubes.

When there is wind in the natural environment, forced convection loss will also appear on the surface of the receiver. This process could be assumed to be the airflow around the tubes. The forced heat transfer coefficient $h_{f,air}$ around the tubes could be obtained by Eq. (11), and the film temperature was selected as the reference temperature of the air,

$$Nu_{f,air} = 0.193Re^{0.618}Pr^{1/3}. \quad (11)$$

The outer wall grid's overall convective heat transfer coefficient could be calculated using $h_{total} = (H_{f,air}^{3.2} + H_{n,air}^{3.2})^{1/3.2}$.

For the outermost grid, the heat flow for the grid to the environment will experience a section of thermal conductivity and a section of convective heat transfer thermal resistance, so the pre-coefficient of the temperature difference between the grid and the environment could be expressed by Eq. (12), which was the reciprocal of the sum of two series heat resistance, where r_o was the outer radius of the tube, m , and r_{NR} was the center radius of the outermost grid ($m = NR$), m ,

$$K_{r,o} = \frac{\Delta Z}{\frac{1}{\lambda \Delta \theta} \ln\left(\frac{r_o}{r_{NR}}\right) + \frac{1}{\Delta \theta r_o h_{total}}}. \quad (12)$$

Thus, the driving equation of the outermost grid was shown in Eq. (13).

$$\begin{aligned} T_{NR,n,k}^{i+1} = & \frac{a\Delta\tau}{r_{NR}\Delta r \ln\left(\frac{r}{r-\Delta r}\right)} \left(T_{NR-1,n,k}^i - T_{NR,n,k}^i\right) \\ & + \frac{K_{r,o}\Delta\tau}{c_p\rho r_{NR}\Delta r\Delta\theta\Delta Z} \left(T_{amb} - T_{NR,n,k}^i\right) \\ & + \frac{\left(q_{NR,m,k}^i\right)_{net} r_o\Delta\tau}{\rho c_p r_{NR}\Delta r} + \frac{a\Delta\tau}{\left(r_{NR}\Delta\theta\right)^2} \\ & \times \left(T_{NR,n+1,k}^i + T_{NR,n-1,k}^i - 2T_{NR,n,k}^i\right) \\ & + \frac{a\Delta\tau}{\left(\Delta Z\right)^2} \left(T_{NR,n,k+1}^i + T_{NR,n,k-1}^i - 2T_{NR,n,k}^i\right) + T_{NR,n,k}^i. \quad (13) \end{aligned}$$

4. The inner wall surface of the tube

The tube's inner wall is in contact with the flowing molten salt, and the molten salt will take away a part of the heat flow from the

inner wall, which will increase the molten salt's temperature. For the convenience of calculation, it is assumed that the temperature of the molten salt is evenly distributed, and the forced convection equation of forced convection in a tube could be used to calculate the molten salt's convective heat transfer coefficient. Here, the more accurate Gnielinski formula was used, and its applicable range is $Re_f = 2300 \sim 10^6$, $Pr_f = 0.6 \sim 10^5$, which is suitable for the heat transfer of molten salt.²⁹ The heat transfer coefficient formulas are shown in the following equations, where c_t is the correction coefficient and f is the Darcy resistance coefficient:

$$Nu_f = \frac{(f/8)(Re - 1000)Pr_f}{1 + 12.7\sqrt{f/8}(Pr_f - 1)} \left[1 + \left(\frac{d}{l}\right)^{2/3}\right] c_t, \quad (14)$$

$$c_t = \left(\frac{Pr_f}{Pr_w}\right)^{0.01}, \quad (15)$$

$$f = (1.82lgRe_f - 1.64)^{-2}. \quad (16)$$

After calculating the molten salt heat transfer coefficient, the pre-coefficient $K_{1,n,k}$ of the temperature difference between the inner surface's grid and the molten salt could be obtained using the following equations, where r_i was the radius of the inner wall and r_1 was the center radius of the innermost grid ($m = 1$):

$$K_{1,n,k} = \frac{\Delta Z}{\frac{1}{\Delta\theta r_i h_i} + \frac{1}{\lambda\Delta\theta} \ln\left(\frac{r_1}{r_i}\right)}. \quad (17)$$

Thus, the control difference equation for the temperature of the inner wall surface grid could be written, as shown in the following equation:

$$\begin{aligned} T_{m,n,k}^{i+1} = & \frac{K_{1,n,k}\Delta\tau}{\rho c_p r \Delta r \Delta\theta \Delta Z} \left(T_{salt,k,b}^i - T_{m,n,k}^i\right) \\ & + \frac{a\Delta\tau}{r\Delta r \ln\left(\frac{r+\Delta r}{r}\right)} \left(T_{m+1,n,k}^i - T_{m,n,k}^i\right) \\ & + \frac{a\Delta\tau}{\left(r\Delta\theta\right)^2} \left(T_{m,n+1,k}^i + T_{m,n-1,k}^i - 2T_{m,n,k}^i\right) \\ & + \frac{a\Delta\tau}{\left(\Delta Z\right)^2} \left(T_{m,n,k+1}^i + T_{m,n,k-1}^i - 2T_{m,n,k}^i\right) + T_{m,n,k}^i. \quad (18) \end{aligned}$$

It should be noted that some grids will have two kinds of boundaries, and in this scenario, the two types of boundary conditions need to be used in combination.

C. Flowchart of the transient program

MATLAB 2017b was used to write a set of calculation routines for the unsteady thermal performance of the receiver based on the governing equations for the temperature of each grid developed in Sec. II B. Figure 4 depicts the program’s flow chart. After meshing and indexing the tubes, the software estimated the angle coefficient between each grid, which was then imported to calculate the net inflow radiant heat flux for each grid. The outermost grid’s natural and forced convection coefficients were then computed, and the pre-coefficient K of each temperature difference could be determined. Then, using the governing equations, the temperature field distribution at each time was computed.

Because the governing equation was written in an explicit difference style, the value of the unit time ($\Delta\tau$) required particular attention.

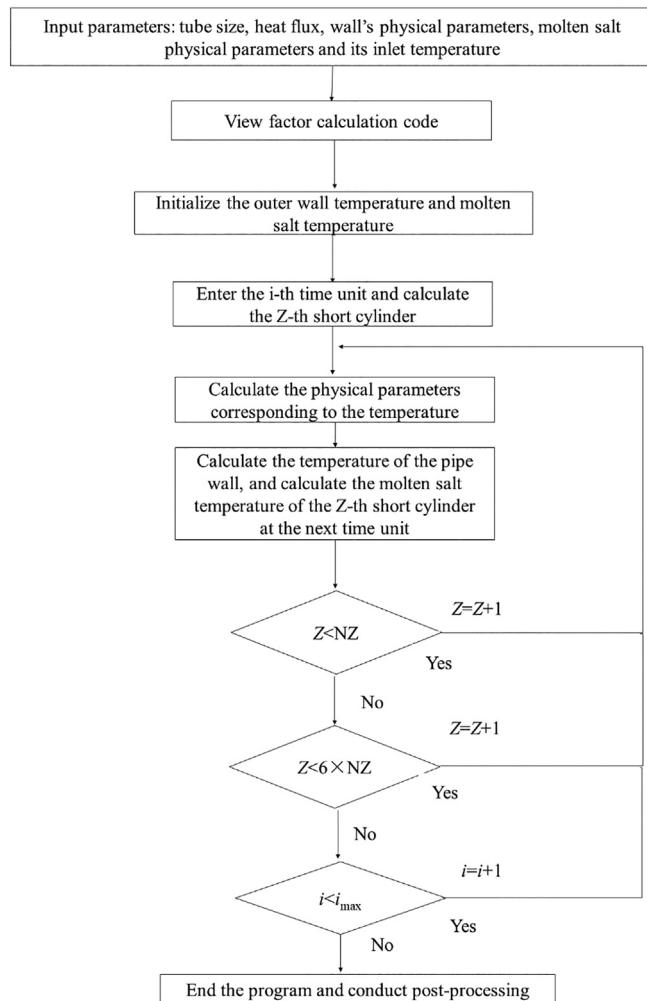


FIG. 4. The flow chart of the calculation program of the unsteady thermal performance of the receiver.

The computation software might diverge if the grid time was too long. The unit time taken in this computation procedure was 0.004 s after testing. The software was declared stable when the temperature field of the receiver stopped changing.

III. RESULTS AND DISCUSS

A. Xenon lamps turned on

Before functioning in the on-site CSP station, the receiver should be warmed and then loaded with salt. This is due to the fact that the molten salt temperature at the receiver’s input is usually around 290 °C, and the molten salt at this temperature may freeze and clog the pipeline when it meets the cold wall. To prevent the receiver from clogging, the entrance temperature of the molten salt at the inlet was adjusted to 400 °C on the lab-scale receiver. At this temperature, the molten salt could be charged straight into the lab-scale receiver without the need for a plug. As a result, no preheating was done in the lab-scale receiver experiment. The surface temperature of the receiver was steady after the molten salt had been cycled for a period, and then turn on the xenon lamp group for heating. Therefore, before the xenon lamp was turned on, the wall temperature and salt temperature of the receiver could be considered uniform, assuming 400 °C. Thus, the wall temperature and salt temperature were both set to 400 °C when simulating the lab-scale receiver at the initial moment.

The benchmark working conditions were molten salt flow 2.3 kg/s, inlet temperature 400 °C, xenon lamp electric power 150 kW, and ambient wind speed 0 m/s. When the xenon lamp was turned on, the molten salt temperature and the receiver’s outer wall temperature would change. This stage is a transient heat exchange process.

The transient thermal performance calculation program was employed to compute the transient temperature distribution of the lab-scale receiver after turning on the xenon lamps, and the transient thermal performance of the lab-scale receiver within 2 min was obtained. Figure 5 presents the maximum outer wall temperature change and the temperature change of molten salt, where the abscissa is time, and the ordinate is the molten salt’s flow length. The heated length of each tube was 0.4 m, and the total flow length of molten salt was 2.4 m. Figure 5(a) depicts the change of the pipes’ maximum outer wall temperature within 2 min. The maximum outer wall temperature was the largest at a flow length of about 2.1 m, about 450 °C. This place was related to the receiver’s heat flux distribution. There was a large heat flux area in the upper half of the last panel of the receiver, which directly led to the higher temperature of the tube at this position. Figure 5(b) describes the temperature change of the molten salt in the lab-scale receiver with its flow within 2 min. The molten salt temperature in the last panel was the highest, and the molten salt temperature gradually increased along with its flow, and the molten salt’s outlet temperature was 403 °C. It could also be found that the maximum outer wall temperature and salt temperature were both stable at about 12 s from Fig. 5; that is to say, the temperature distribution of the lab-scale receiver did not change after 12 s. This phenomenon can also be found in Fig. 6. Figure 6 shows the curve of the maximum outer wall temperature at some positions of the receiver over time, where Z represented the flow length of the molten salt. From this curve, it could be clearly seen that when the time reaches about 12 s, the maximum outer wall temperature was no longer changing after 12 s. In addition, the average heating rate of the maximum outer wall temperature at the fluid flow length of 1 m was 3.2 °C/s.

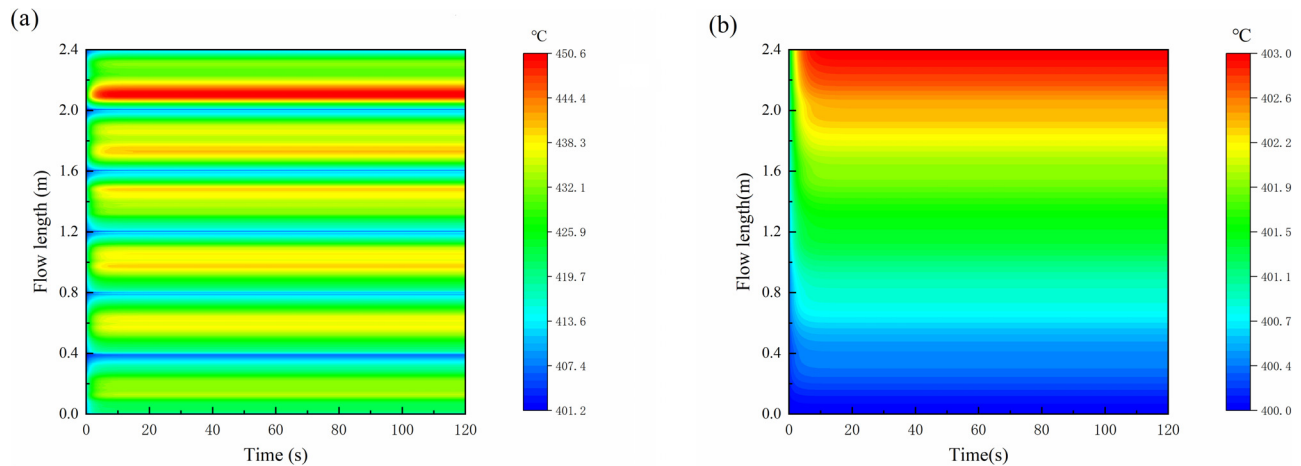


FIG. 5. The maximum outer wall temperature and molten salt temperature change of the receiver after turning the lamps. (a) The variation of maximum outer wall temperature and (b) the temperature variation of the molten salt.

In addition, Fig. 7 draws the change curves of the molten salt temperature and the maximum outer wall temperature with the flow of molten salt after turning on the xenon lamps. The temperature of the molten salt and outer wall changed rapidly between $\tau = 1-3$ s, and the molten salt temperature and maximum outer wall temperature no longer varied after $\tau = 10$ s. Figure 7 also compares the maximum outer wall temperature when it was stable using the transient models and the results obtained by the steady-state calculation program by Zhou *et al.*¹⁴ It was clear that the maximum outer wall temperature obtained by the two programs was basically the same, with a small error. However, in comparing the salt temperature, the molten salt's temperature rise of the receiver obtained was 5.2°C by the experimental measurement, while the temperature rise obtained by the unsteady state calculation program was 3°C , with a difference of 2.2°C .

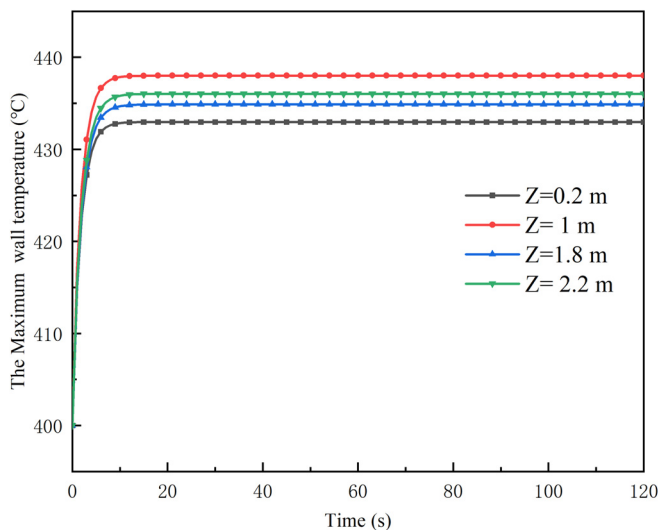


FIG. 6. The maximum outer wall temperature change curve at different positions of the tube.

However, the molten salt's temperature rise was not large enough due to the low power of the xenon lamps, and the error of the K-type thermocouple itself was significant, about 1.5 K , which might cause such a significant error. Therefore, the accuracy of the calculation program for the receiver's unsteady thermal performance was acceptable.

To explore the temperature difference between the inner and outer walls of the tube, Fig. 7(c) shows the change of the temperature difference between the inner and outer walls at grids perpendicular to the projected light, whose azimuth angle was $\theta = 0^\circ$ and [see Fig. 2(b)]. Similarly, it could be seen that the temperature difference changed rapidly between $\tau = 1-3$ s, and the temperature difference basically no longer changed after 10 s. When it was stable, the maximum temperature difference between the inner and outer walls was close to 8°C . The temperature difference was small and would not cause sizeable thermal stress, and the main reason was the heat flux density on the receiver's surface was small.

B. Effect of the molten salt flow

1. The molten salt flow changed from 2.3 to 2.0 kg/s

To explore the effect of the molten salt flow rate on the wall's temperature and molten salt temperature, this section instantly adjusted the flow rate from 2.3 to 2.0 kg/s based on the benchmark conditions. After changing the salt flow rate, the transient thermal performance of the receiver was calculated by modifying the molten salt flow rate in the transient code.

Figures 8(a) and 8(b) shows the curves of the molten salt temperature and the maximum outer wall temperature of the receiver along with the molten salt flow at different times after the molten salt flow was adjusted from 2.3 to 2.0 kg/s. It could be found that the maximum outer wall temperature changed between $\tau = 60-65$ s, and then the temperature distribution became basically stable after $\tau = 65$ s. Compared with Sec. III A, the maximum outer wall temperature changed smaller and stabilized faster. After the receiver was stabilized, the molten salt temperature and the maximum outer wall temperature were increased compared to the molten salt flow rate of 2.3 kg/s.

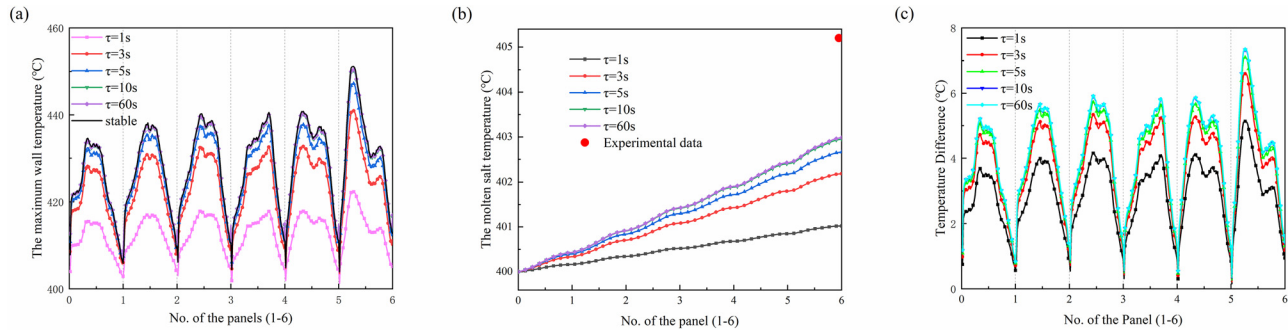


FIG. 7. The change curves of the maximum outer wall temperature and molten salt temperature of the lab-scale receiver after the xenon lamps were turned on (a) the maximum outer wall temperature and (b) the molten salt temperature. (c) The temperature difference between inner and outer wall at $\theta = 0^\circ$.

This was due to the fact that the light load remained unchanged, making the temperature rise of less molten salt became higher, causing the pipe wall temperature to rise. Therefore, when the fluid flow rate decreased, the wall temperature increased, and vice versa.

Figure 8(c) shows the curve of the temperature difference between the inner and outer walls of the grids ($\theta = 0^\circ$) at different times after the molten salt flow was adjusted from 2.3 to 2.0 kg/s. The change of the temperature difference was extremely small and relatively slow, so it would not produce sizeable thermal stress.

Figures 9(a) and 9(b), respectively, depicts the change curves of the molten salt temperature and the maximum outer wall temperature with time (60–120 s) at some locations on the lab-scale receiver when the flow rate of the molten salt varied from 2.3 to 2.0 kg/s, for example, the central section at the first tube (0.2 m), the central section of the third tube (1 m), the central section of the fifth tube (1.8 m), and the sixth tube central section (2.2 m). It could be seen that among the four locations, the maximum outer wall temperature at $Z = 1$ m was the largest, which was begotten by the uneven heat flux distribution. This phenomenon was absent in the molten salt temperature curve, and the molten salt temperature rose gradually with its flow. In addition, when the flow rate of the molten salt changed from 2.3 to 2.0 kg/s, the time for the receiver to stabilize was about 8 s, and the temperature distribution of the receiver became stable again after 8 s. Compared with the time when the xenon lamp was just turned on, this reaction was more rapid, mainly because the temperature change at this stage was

smaller. After calculation, the heating rate of the maximum outer wall temperature at a flow length of 1 m of the molten salt was 0.47°C/s from the molten salt flow rate changing to the temperature of the receiver reaching stable again, and the heating rate of corresponding molten salt was 0.02°C/s . In addition, the average heating rate of the maximum outer wall temperature at the salt flow length of 2.2 m was 0.45°C/s , and the average heating rate of the molten salt here was 0.05°C/s . It could be found that the change of the wall temperature of the receiver had a more significant relationship with the heat flow distribution, and the molten salt temperature evolution had a closer relationship with the flow length of the molten salt.

2. Continuous change of the molten salt flow rate

The flow rate of the molten salt was adjusted to 1.8, 1.6, and 1.4 kg/s, in turn, after the molten salt flow rate was adjusted to 2.0 kg/s, and this setting corresponded to the variable working condition experiment by Zhou *et al.*¹⁴ The changing curves of the molten salt temperature and maximum outer wall temperature at some specific positions of the receiver when the flow rate of the receiver changed from 2.3 to 1.4 kg/s continuously are presented in Fig. 10. The selected positions were the same as those in Sec. III A, and it was also true for the subsequent results. From Figs. 10(a) and 10(b), it can be found that the maximum outer wall temperature of the tube and the molten salt temperature gradually increased with the molten salt flow rate varying,

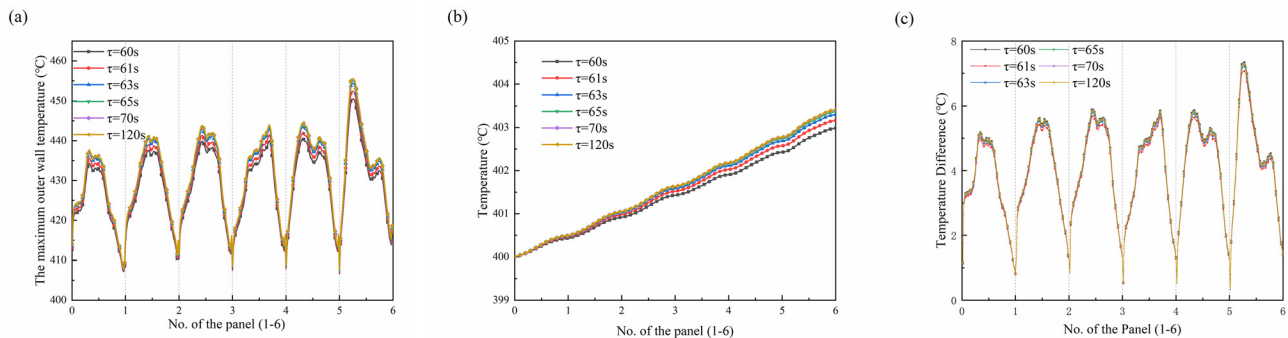


FIG. 8. The maximum outer wall temperature, salt temperature, and temperature difference change of the lab-scale heat receiver when the molten salt flow was changed from 2.3 to 2.0 kg/s (a) the maximum outer wall temperature (b) the molten salt temperature. (c) Temperature difference between inner and outer wall at $\theta = 0^\circ$.

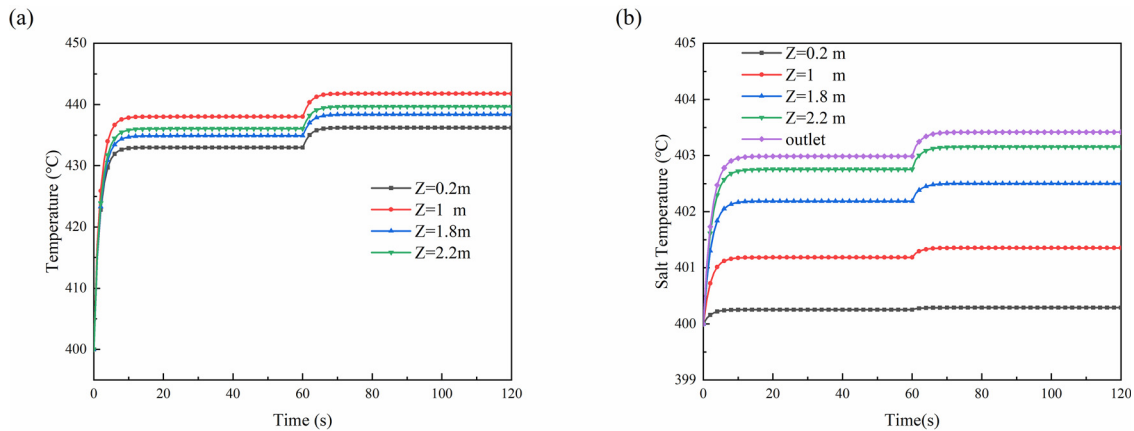


FIG. 9. When the molten salt flow rate is changed from 2.3 to 2.0 kg/s, the temperature of the molten salt in the receiver changes (a) the maximum outer wall temperature and (b) the molten salt temperature.

and the receiver reached a new stable level after about 8 s once the molten salt flow rate changed. After calculation, the change values of the molten salt outlet temperature when the molten salt flow changes sequentially were, respectively, 403.41, 403.78, 404.23, and 404.81 °C, and the maximum outer wall temperature at the molten salt flow length of 1 m were 441.79, 444.93, 448.78, and 453.69 °C, respectively. Figure 11 shows the comparison of the experimental and simulation results based on a variable molten salt flow rate, wherein the experimental data are the temperature difference of the molten salt temperature between the inlet and outlet of the receiver. It can be found that the molten salt outlet temperature and the molten salt flow rate had a linear relationship and the experimental and simulated data have similar trends and good consistency, and the specific deviation is and the specific deviation is caused by the deviation of the measurement. The temperature difference Δt between the inlet and outlet of molten salt in the receiver, also called the temperature rise of molten salt, can be calculated by Eq. (19), where Q_{salt} is the mass flow of molten salt, c is the specific heat capacity, η is the average heat absorption rate of the

receiver, Φ is the energy projected by the xenon lamp onto the receiver, $Q_{c,loss}$ is the total convective heat transfer loss, and $Q_{r,loss}$ is the energy loss through radiation. When the flow rate changes, the right-hand side of Eq. (18) decreases slightly and can be considered to be constant, so the temperature rise of the molten salt and the flow rate of the molten salt are approximately inversely proportional, namely, $\Delta t \propto \frac{1}{q_{mass}}$. Both experimental and simulated values were curve-fitted using this relationship, and the results are shown in Fig. 11. It can be found that the temperature rise of the molten salt and the flow of the molten salt in the experimental and simulated results are inversely proportional functions, and the goodness of fit of the experimental results was 0.932, while the goodness of fit of the simulation results was 0.998. It can be seen that the difference between the experimental and simulation results was basically between 2 and 3 °C. The coefficients of the fitting curve equation are different, which means that the heat absorbed by the molten salt calculated by the simulation was lower than the actual absorbed energy, which is mainly caused by the overestimation of the convection heat loss. This is

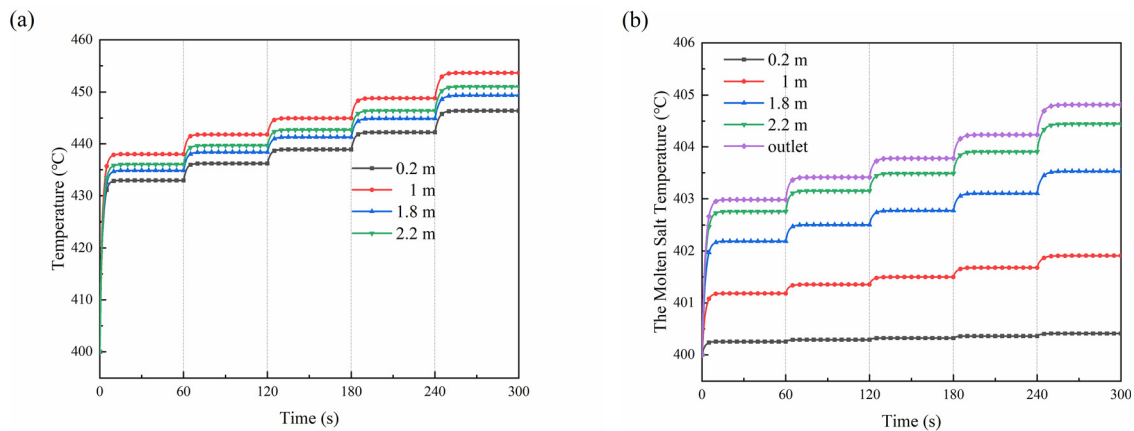


FIG. 10. The maximum outer wall temperature and the molten salt change in some positions when the molten salt flow rate changes from 2.3, 2.0, 1.8, 1.6, 1.4 kg/s in sequence: (a) the maximum outer wall temperature and (b) the molten salt temperature.

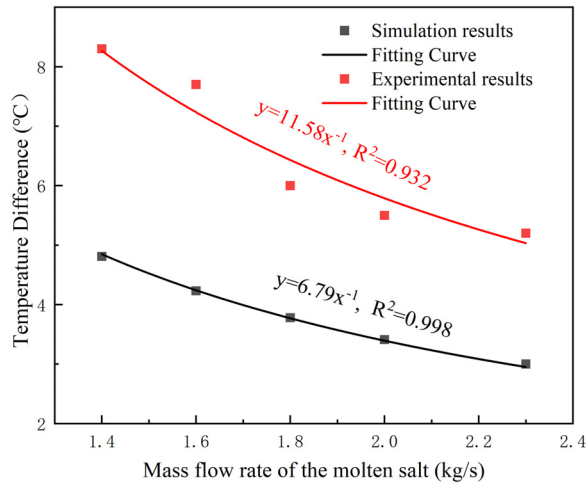


FIG. 11. The relationship between molten salt flow rate and molten salt temperature rise.

because the projection energy provided by the xenon lamp was small, and when calculating the energy loss, the little error caused by the selected calculation formula would have an excessive impact on the result, but it would not occur in the calculation of the on-site receiver,

$$Q_{salt} \cdot c \cdot \Delta t = \eta \cdot \Phi_{input} - Q_{c,loss} - Q_{r,loss}. \quad (19)$$

C. Effect of the xenon lamp power

1. The xenon lamp power changes from 100% to 80%

To explore the heat flux distribution's effect on the receiver's temperature distribution of the tube wall and the molten salt, the xenon lamp's electric power was adjusted during the experiment to modify the receiver surface's heat flux distribution. This section studied changes in the receiver's temperature distribution when the xenon lamps group's electric power varied from 100% to 80%. Through measurement, when the electric power rate of the xenon lamp group dropped from 100% to 80%, the heat flux it produced became 85.18% of the original. The new heat flux distribution obtained was imported into the receiver's transient thermal performance calculation program

to predict the change in the receiver's thermal performance at this stage.

Figures 12(a) and 12(b) show the curves of the molten salt temperature and the maximum outer wall temperature at different times after the xenon lamps' electric power rate dropped from 100% to 80%. It could be seen that the maximum outer wall temperature of the receiver varied between $\tau = 60-65$ s, and the temperature was basically stable after 65 s. After it was stabilized, the molten salt temperature and maximum outer wall temperature were lower than when the xenon lamps had 100% electric power because the smaller heat flux density could make the molten salt's outlet temperature rise lower when the molten salt flow rate was constant, which caused the pipes' wall temperature to drop.

Figure 12(c) shows the curve of the temperature difference between the inner and outer walls at different times when the xenon lamps' electric power rate was adjusted from 100% to 80%. When the electric power of the xenon lamp dropped, the temperature difference became smaller, and the temperature difference changed rapidly between 60 and 61 s, and the temperature changed slowly between 61 and 65 s. It could be found that after the receiver was stabilized, the temperature difference became smaller than before. Therefore, when the heat flux density became smaller, the temperature difference between the inner and outer walls of the receiver became smaller, thereby reducing the thermal stress.

Figures 13(a) and 13(b), respectively, depict the molten salt temperature and maximum outer wall temperature at some positions after the xenon lamp electric power rate was adjusted from 100% to 80% over time (60–120 s). It could be seen that when the xenon lamps' electric power was modified from 100% to 80%, the time for the receiver to stabilize was about 7 s, which was slightly faster than that when the flow rate of molten salt was changed. After calculation, the maximum temperature drop rate of the outer wall at the section of the molten salt flow length of 1 m was 0.88°C/s , whereas the temperature drop rate of the molten salt was 0.03°C/s . Besides, the average cooling rate of the maximum outer wall temperature at a flow length of 2.2 m was 0.85°C/s , whereas the average cooling rate of molten salt was 0.07°C/s .

2. The electric power of the xenon lamp group changes continuously

After the electric power rate of the xenon lamps was adjusted to 80%, the electric power was adjusted to 60%, 40%, and 20% in turn.

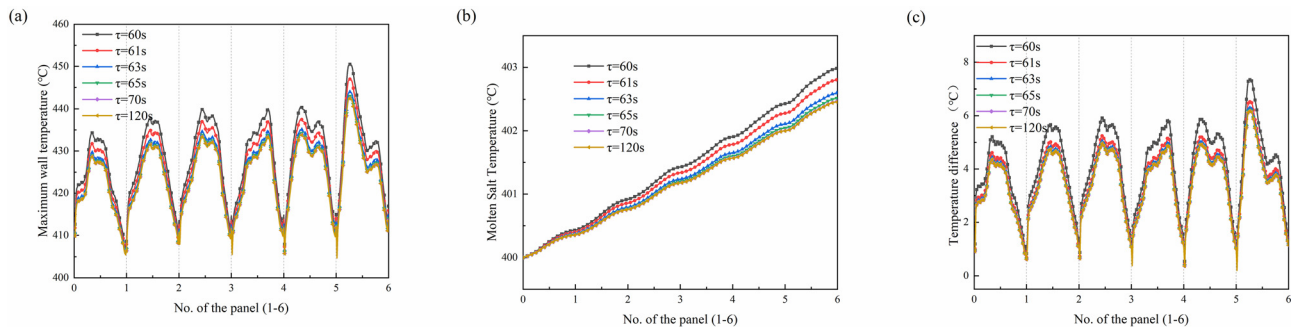


FIG. 12. The maximum outer wall temperature, molten salt temperature, and temperature difference change after the electric power of the xenon lamps were adjusted from 100% to 80%: (a) the maximum outer wall temperature and (b) the molten salt temperature. (c) Temperature difference between inner and outer wall at $\theta = 0^\circ$.

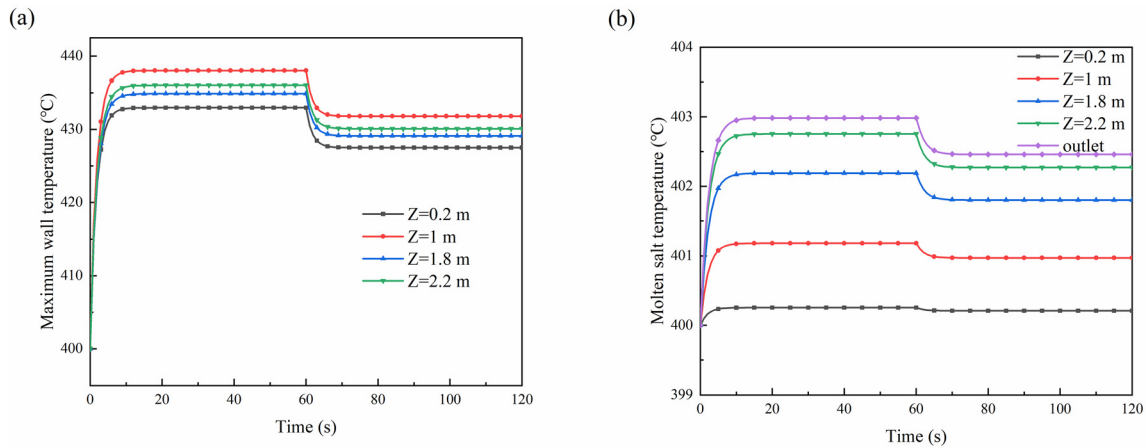


FIG. 13. The change of the molten salt temperature of the heat receiver after the electric power of the xenon lamp is adjusted from 100% to 80%: (a) the maximum outer wall temperature and (b) the molten salt temperature.

The heat flux density corresponding to 20%, 40%, and 60% electric power were 64.64%, 43.30%, and 23.37% of the heat flux density corresponding to 100% electric power. Figures 14(a) and 14(b), respectively, show the change curves of the molten salt temperature and maximum outer wall temperature at some specific locations of the receiver when the electric power of the xenon lamp changed from 100% to 20%. From Figs. 14(a) and 14(b), it can be found that the molten salt temperature and the maximum outer wall temperature were gradually decreased when the electric power of the xenon lamps varied, and the time for the receiver to stabilize again was about 7 s. After calculation, when the electric power of the xenon lamp changed sequentially, the molten salt outlet temperature was 402.47, 401.38, 400.25, and 399.58 °C, respectively, and the maximum outer wall temperature at a flow length of 1 m was 431.79, 418.79, 405.35, and 397.32 °C, respectively. When the xenon lamps' electric power was set to 20%, the molten salt outlet temperature, and the tubes' maximum outer wall temperature were both lower than the molten salt inlet temperature (400 °C), which meant that the heat loss was greater than the absorbed

energy of the receiver. In addition, the relationship between the molten salt temperature rise and the heat flux density ratio is shown in Fig. 15. It could be seen that the relationship between the two was approximately linear, which was also similar to the relationship diagram obtained by Zhou *et al.*¹⁴ When the electric power of the xenon lamp changed linearly, the energy projected on the surface of the receiver changed approximately linearly. However, when the electric power of the xenon lamp decreased, the surface temperature of the receiver did not change much (not exceeding 30 °C), but the absorption rate and heat loss were reduced, so finally the relationship between the temperature rise of the molten salt and the xenon lamps electric power was linear.

D. Effect of the wind velocity

1. Wind velocity changing from 0 to 2 m/s

To explore the impact of ambient wind speed on the tube wall temperature and molten salt, this section instantly adjusted the wind

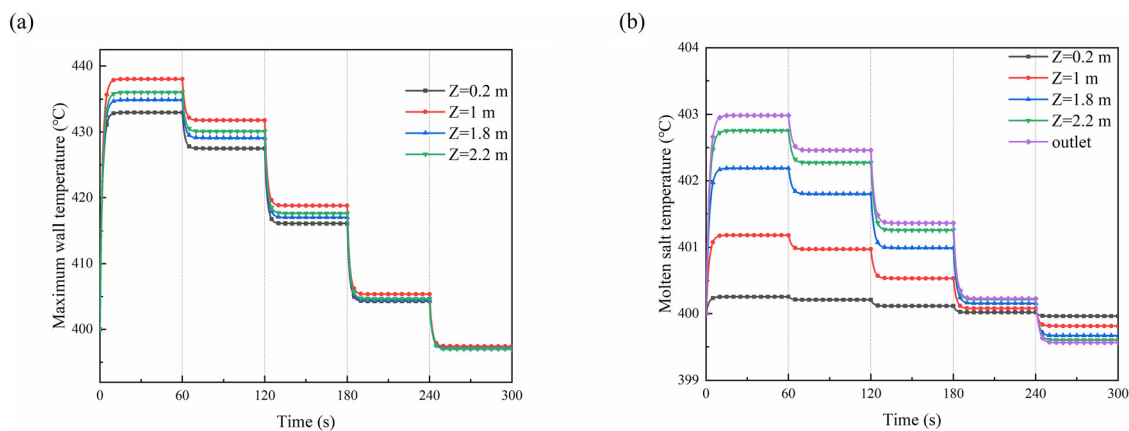


FIG. 14. The change curve of the molten salt temperature of the heat receiver when the electric power of the xenon lamp group changes continuously: (a) the maximum outer wall temperature (b) the molten salt temperature.

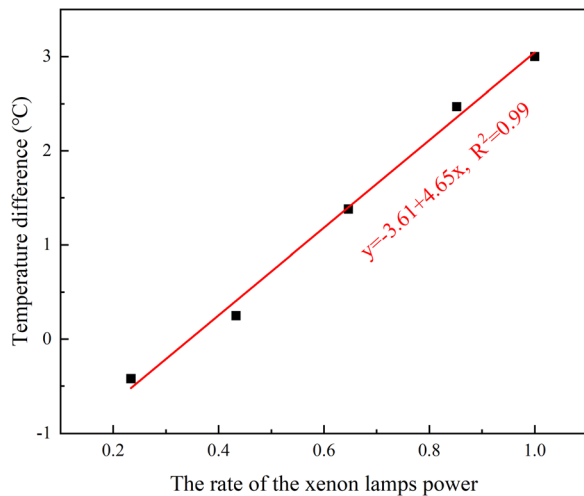


FIG. 15. The relationship between the temperature rise of the molten salt and the ratio of the heat flux density.

speed from 0 to 2 m/s. Then, the calculation program was applied to compute the lab-scale receiver's transient thermal performance after the wind speed was changed.

Figures 16(a) and 16(b) show the curve of the molten salt temperature and maximum outer wall temperature at different times when the wind velocity varies from 0 to 2 m/s. The maximum outer wall temperature varied between $\tau = 60\text{--}65$ s, and the temperature reached basically stable after 65 s. After the receiver was stabilized, the molten salt temperature and maximum outer wall temperature were reduced compared to the benchmark condition results. The energy lost by the receiver would increase when there was wind speed, which led to a decrease in the heat absorbed by the molten salt.

Figure 16(c) shows the curve of the temperature difference between the inner and outer walls of the tube at $\theta = 0^\circ$ at different times after the ambient wind velocity varies from 0 to 2 m/s. It could be seen that the temperature difference became smaller after the wind

velocity became 2 m/s, and the change was faster between 60 and 61 s, but the temperature changed slowly between 61 and 65 s. After the receiver was stabilized, it could be seen that the temperature difference became smaller than the benchmark's result. Therefore, the tubes' temperature difference would become smaller when the ambient wind velocity increased.

Figures 17(a) and 17(b), respectively, show the molten salt temperature and the maximum outer wall temperature at some locations on the lab-scale receiver with time (60–120 s) after the ambient wind velocity changed from 0 to 2 m/s. It could be seen that the time for the receiver to stabilize was about 9 s once the ambient velocity varied. The maximum outer wall temperature at $Z = 1$ m was 0.44°C/s when the wind velocity varied from 0 to 2 m/s, where the cooling rate of the molten salt was 0.05°C/s . In contrast, the average cooling rate of the maximum outer wall temperature at $Z = 2.2$ m was 0.49°C/s , whereas the average cooling rate of molten salt was 0.11°C/s .

2. Continuous changes in ambient wind speed

In order to study the effect of the wind velocity on the transient performance of the solar receiver, the ambient wind speed was adjusted to 4, 6, 8, and 10 m/s in turn. This setting corresponded to the variable working condition experiment in Zhou *et al.*¹⁴ Figure 18, respectively, show the changes in the molten salt temperature and maximum outer wall temperature at some specific locations when the ambient wind speed changed from 0 to 10 m/s. From Figs. 18(a) and 18(b), it can be found that as the ambient wind velocity changed, the molten salt temperature and the tubes' maximum outer wall temperature were gradually decreasing. The time for the receiver to stabilize was about 9 s when the ambient wind speed varied. When the ambient wind velocity changed sequentially, the molten salt outlet temperature was 401.87, 401.10, 400.49, 400, 399.47 °C, respectively, and the maximum outer wall temperature at a flow length of 1 m was 434.08, 431.36, 429.16, 427.24, and 425.52 °C, respectively. It could be found that the molten salt outlet temperature and the maximum outer wall temperature when the wind velocity was set to 10 m/s were both lower than the molten salt inlet temperature (400 °C), that is to say, the heat dissipated from the receiver was greater than the energy absorbed.

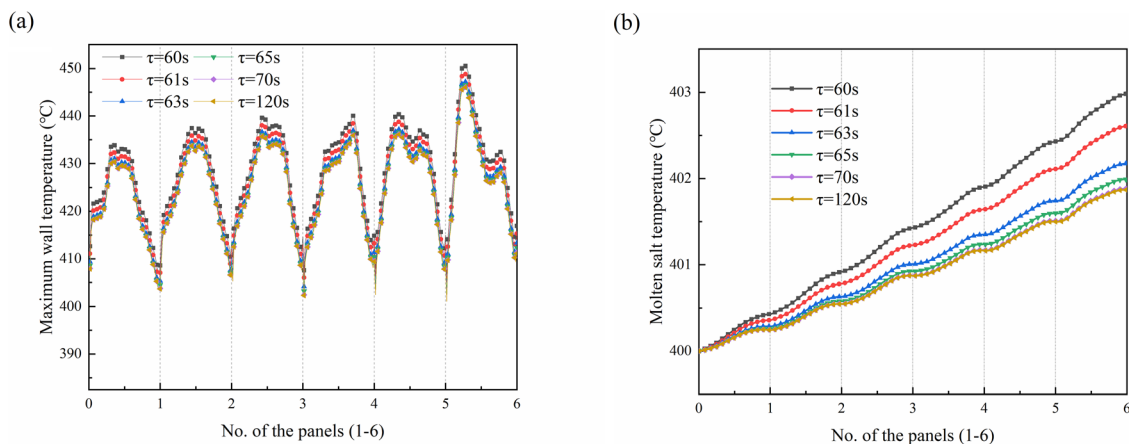


FIG. 16. The maximum outer wall temperature, molten salt temperature, and temperature difference change when the wind speed changed from 0 to 2 m/s: (a) the maximum wall temperature and (b) the molten salt temperature. (c) Temperature difference between inner and outer wall at $\theta = 0^\circ$.

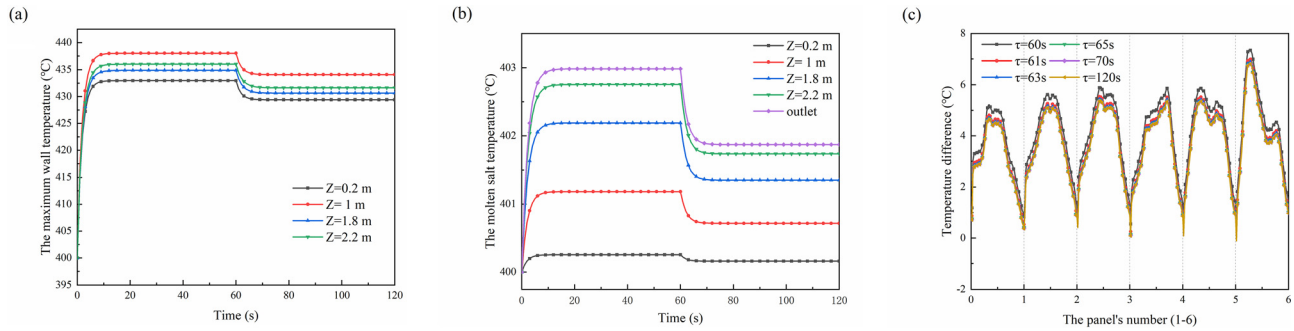


FIG. 17. The change curve of the molten salt temperature in the heat receiver with time when the wind speed changes from 0 to 2 m/s: (a) the maximum outer wall temperature and (b) the molten salt temperature.

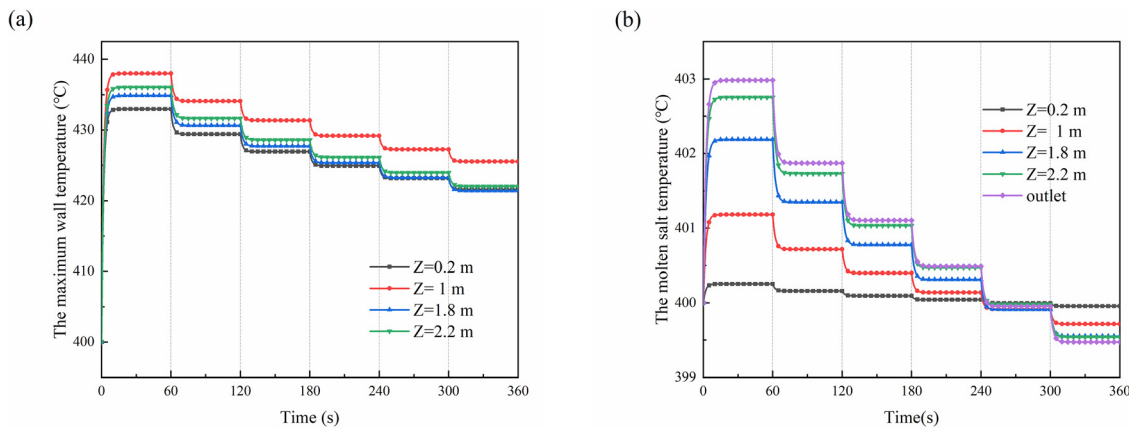


FIG. 18. The temperature of the molten salt in the heat receiver changes with time when the ambient wind speed changes: (a) the maximum outer wall temperature and (b) the molten salt temperature.

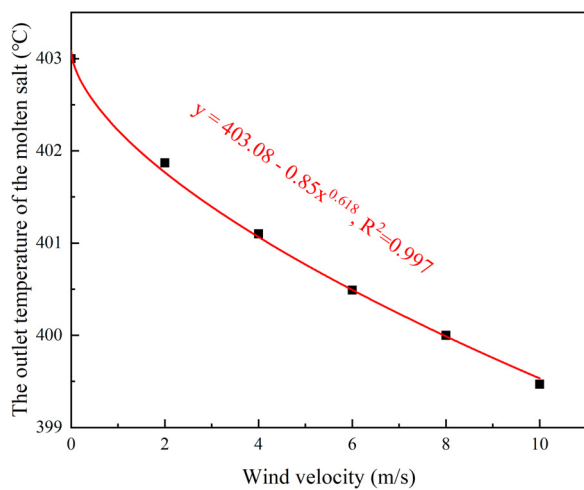


FIG. 19. The relationship between the temperature rise of the molten salt and the ambient wind speed.

In addition, the relationship between the molten salt’s outlet temperature and the ambient wind speed is shown in Fig. 19. When the ambient wind speed changes, the natural convection loss, radiation loss, and absorbed heat change are small, it can be assumed to remain unchanged, so the total convection loss is mainly related to the Reynolds number, $Q_{c,loss} \propto Re^{0.618}$, it can be considered that the temperature difference Δt between the inlet and outlet molten salt and $u_{\infty}^{0.618}$ have approximate linear relationship according to Eq. (19), where u_{∞} is the ambient wind speed. When this relationship was used to fit the simulated results, a formulation of $\Delta t = 3.08 - 0.85u_{\infty}^{0.618}$ can be obtained, and the goodness of fit is 0.997, so the above assumptions can be considered reasonable.

IV. SUMMARY AND CONCLUSIONS

In this article, a collection of transient calculation programs was created and then utilized to determine the transient thermal performance of a lab-scale receiver under various situations. When the molten salt flow rate changed, the heat flux changed, and the ambient wind speed changed, the lab-scale receiver’s transient thermal performance was reviewed. The following were the major findings reached:

- (1) Under the benchmark condition, the molten salt temperature and maximum outer wall temperature of the lab-scale receiver were steady at about 12 s after turning on the xenon light. After stabilization, the molten salt outlet temperature of the lab-scale receiver was around 403 °C, and the molten salt outlet temperature rise was 3 °C, which was 2.2 °C higher than the experimental results. The maximum outer wall temperature development curve was very near to the result generated by the steady-state calculation software, demonstrating the calculation program's correctness for the receiver's transient thermal performance.
- (2) When the molten salt flow rate was changed from 2.3 to 2.0 kg/s, the temperature distribution in the lab-scale receiver became steady after about 8 s. When the molten salt flow rate was reduced, the temperature of the molten salt at the receiver's outlet progressively increased. Furthermore, the molten salt temperature rise was discovered to have an inversely proportional function with the molten salt flow rate.
- (3) The tube's temperature distribution became stable again after modifying the xenon lights' electric output to vary the surface's heat flux distribution of the receiver. The molten salt exit temperature steadily drops as the heat flow density decreases. The receiver's molten salt temperature rise exhibited a linear connection with the receiver's surface heat flux rate, according to the research.
- (4) When the ambient wind velocity changed, the temperature distribution of the lab-scale receiver became steady at around 9 s. The molten salt outlet temperature of the receiver gradually fell as the ambient wind speed rose. The molten salt temperature rise was shown to have a relationship of $\Delta t = 3.08 - 0.85u_{\infty}^{0.618}$ with the ambient wind velocity.

ACKNOWLEDGMENTS

This research did not receive any specific grant from funding agencies in the public, commercial, or not-for-profit sectors.

AUTHOR DECLARATIONS

Conflict of Interest

The authors have no conflicts to disclose.

DATA AVAILABILITY

The data that support the findings of this study are available from the corresponding author upon reasonable request.

REFERENCES

- ¹C. K. Ho, *Sol. Energy* **152**, 38 (2017).
- ²A. Peinado Gonzalo, A. Pliego Marugán, and F. P. García Márquez, *Appl. Energy* **255**, 113893 (2019).
- ³L. Xu, W. Stein, J.-S. Kim, Y. C. S. Too, M. Guo, and Z. Wang, *Appl. Therm. Eng.* **141**, 1035–1047 (2018).
- ⁴L. Xu, W. Stein, J.-S. Kim, and Z. Wang, *Renewable Energy* **120**, 550–566 (2018).
- ⁵Z. Liao, X. Li, C. Xu, C. Chang, and Z. Wang, *Renewable Energy* **62**, 747 (2014).
- ⁶M. R. Rodríguez Sanchez, M. Venegas Bernal, C. Marugán Cruz, and D. Santana, *Renewable Energy and Power Quality Journal* **1**, 128–133 (2013).
- ⁷T. Conroy, M. N. Collins, J. Fisher, and R. Grimes, *Appl. Energy* **230**, 590–614 (2018).
- ⁸S. S. Mostafavi Tehrani and R. A. Taylor, *Appl. Energy* **179**, 698–715 (2016).
- ⁹M. R. Rodríguez-Sánchez, C. Marugán-Cruz, A. Acosta-Iborra, and D. Santana, *Appl. Therm. Eng.* **73**(1), 993–1005 (2014).
- ¹⁰M. R. Rodríguez-Sánchez, A. Sánchez-González, A. Acosta-Iborra, and D. Santana, *AIP Conf. Proc.* **1850**, 030043 (2017).
- ¹¹J. Ballestrín and R. Monterreal, *Energy* **29**(5–6), 915–924 (2004).
- ¹²Q. Zhang, X. Li, Z. Wang, C. Chang, and H. Liu, *Renewable Energy* **50**, 214–221 (2013).
- ¹³H. Zhou, Y. Li, Y. Zhu, W. Fang, D. Liu, M. Zhou, and K. Cen, *J. Renewable Sustainable Energy* **12**(4), 043705 (2020).
- ¹⁴H. Zhou, Y. Li, M. Zhou, D. Liu, Y. Zhu, and W. Fang, *J. Energy Eng.* **147**(1), 04020074 (2021).
- ¹⁵X. Li, W. Kong, Z. Wang, C. Chang, and F. Bai, *Renewable Energy* **35**(5), 981–988 (2010).
- ¹⁶Y. Li, H. Zhou, Y. Zuo, and M. Zhang, *Renewable Energy* **182**, 602–614 (2022).
- ¹⁷M. Fernández-Torrijos, C. Sobrino, J. A. Almendros-Ibáñez, C. Marugán-Cruz, and D. Santana, *Int. J. Heat Mass Transfer* **139**, 503–516 (2019).
- ¹⁸M. Fernández-Torrijos, C. Sobrino, C. Marugán-Cruz, and D. Santana, *Appl. Therm. Eng.* **178**, 115528 (2020).
- ¹⁹L. Xu, Z. F. Wang, G. F. Yuan, F. H. Sun, and X. L. Zhang, *Energy Procedia* **69**, 218–225 (2015).
- ²⁰L. Xu, F. Sun, L. Ma, X. Li, D. Lei, G. Yuan, H. Zhu, Q. Zhang, E. Xu, and Z. Wang, *Sol. Energy* **179**, 195 (2019).
- ²¹L. Xu, Z. Wang, X. Li, G. Yuan, F. Sun, and D. Lei, *Sol. Energy* **95**, 65 (2013).
- ²²L. Xu, F. Sun, L. Ma, X. Li, G. Yuan, D. Lei, H. Zhu, Q. Zhang, E. Xu, and Z. Wang, *Energy* **162**, 1077 (2018).
- ²³X. Shen, J. Lu, J. Ding, and W. Wang, *Energy Procedia* **158**, 541 (2019).
- ²⁴G. Augsburg and D. Favrat, *Sol. Energy* **87**, 42 (2013).
- ²⁵J. García, Y. C. Soo Too, R. V. Padilla, A. Beath, J.-S. Kim, and M. E. Sanjuan, *Renewable Energy* **121**, 355 (2018).
- ²⁶C. Balaji, B. Srinivasan, and S. Gedupudi, *Heat Transfer Engineering*, edited by C. Balaji, B. Srinivasan, and S. Gedupudi (Academic Press, 2021), pp. 15–64.
- ²⁷G. W. Lopez, *J. Propul. Power* **15**, 424 (1999).
- ²⁸S. W. Churchill, *Heat Exchange Handbook* (Hemispheres Publishing, New York, 1983).
- ²⁹V. Gneilinski, *Int. J. Chem. Eng.* **16**, 359 (1976).